ORIGINAL PAPER

CrossMark

Experimental Analysis of Hydraulic Fracture Growth and Acoustic Emission Response in a Layered Formation

Li Ning[1] · Zhang Shicheng[1] · Zou Yushi[1] · Ma Xinfang[1] · Wu Shan[1] · Zhang Yinuo[1]

Abstract

Microseismic/acoustic emission (AE) monitoring is an essential technology for understanding hydraulic fracture (HF) geometry and stimulated reservoir volume (SRV) during hydraulic fracturing in unconventional reservoirs. To investigate HF growth mechanisms and features of induced microseismic/AE events in a layered formation, laboratory fracturing experiments were performed on shale specimens (30 cm × 30 cm × 30 cm) with multiple bedding planes (BPs) under triaxial stresses. AE monitoring was used to reveal the spatial distribution and hypocenter mechanisms of AE events induced by rock failure. Computerized tomography scanning was used to observe the internal fracture geometry. Experimental results showed that the various HF geometries could be obviously distinguished based on injection pressure curves and AE responses. Fracture complexity was notably increased when vertically growing HFs connected with and opened more BPs. The formation of a complex fracture network was generally indicated by frequent fluctuations in injection pressure curves, intense AE activity, and three-dimensionally distributed AE events. Investigations of the hypocenter mechanisms revealed that shear failure/event dominated in shale specimens. Shear and tensile events were induced in hydraulically connected regions, and shear events also occurred around BPs that were not hydraulically connected. This led to an overestimation of HF height and SRV in layered formations based on the AE location results. The results also showed that variable injection rate and using plugging agent were conducive in promoting HF to penetrate through the weak and high-permeability BPs, thereby increasing the fracture height.

Keywords Layered formation · Hydraulic fracture growth · Acoustic emission · Shear event · Stimulated reservoir volume

List of symbols

E	Young's modulus
N	Poisson's ratio
T	Tensile strength
σ_c	Compressive strength
Σ_h	Horizontal minimum principal stress
Σ_H	Horizontal maximum principal stress
Σ_v	Vertical stress
K_h	Permeability parallel to BP
K_v	Permeability perpendicular to BP
Q	Injection rate
M	Fluid viscosity
Λ	Proportion of dilatational first motions
T	Injection time
P_b	Breakdown pressure
N_{AE}	Accumulative number of AE events

✉ Zou Yushi
  zouyushi@126.com

1 State Key Laboratory of Petroleum Resource
   and Prospecting, China University of Petroleum (Beijing),
   Beijing 102249, China

1 Introduction

Hydraulic fracturing is an essential technique for developing ultra-low permeability unconventional reservoirs. Due to the existence of geological discontinuities such as natural fractures (NFs), bedding planes (BPs), and faults, etc., both the growth mechanism and geometry of hydraulic fractures (HFs) become complicated during reservoir stimulation. Microseismic fracture mapping results have indicated that multistage fracturing of a horizontal well can lead to the generation of a complex fracture network in shale formations (Maxwell et al. 2002; Fisher et al. 2005). Further, field data have revealed a correlation between well production and stimulated reservoir volume (SRV) calculated from the spatial distribution of microseismic events. Generally, a larger SRV and more complex fracture geometry tend to

result in improved well performance (Cipolla et al. 2008, 2011). Therefore, investigating the growth mechanism of HFs is important for optimizing stimulation strategies for unconventional reservoirs.

In unconventional reservoirs, the SRV means a complex three-dimensional fracture network which is generated by HFs simultaneously activating a NF system in the horizontal direction and multiple BPs in the vertical direction. The growth mechanism of the complex fracture network has been extensively studied experimentally and theoretically. In previous decades, laboratory-based fracturing experiments were performed to investigate intersection behavior when a HF encountered a preexisting fracture (Warpinski and Teufel 1984; Beugelsdijk et al. 2000; Casas et al. 2006; Zhou et al. 2008; Olson et al. 2012). Further, some criteria regarding the interaction between HFs and NFs have been proposed on the basis of various assumptions (Warpinski and Teufel 1984; Renshaw and Pollard 1995; Potluri et al. 2005; Zhang and Jeffrey 2007; Weng et al. 2011). Experimental and theoretical results have shown that an HF tends to divert along and activate a NF system at low horizontal differential stresses and intersection angles. Under these conditions, the complexity of the fracture geometry is significantly increased in the horizontal direction. Additionally, the existence of numerous BPs in the vertical direction is another distinct feature of unconventional reservoirs such as shale and tight sandstone. These natural laminated structures greatly influence the vertical growth behavior of HFs. Thiercelin et al. (1987) suggested that four interaction modes—penetration, diversion, offset, and termination—can occur when a vertically growing HF approaches a BP in a layered formation. When the HF penetrates and opens multiple BPs, the fracture network complexity is increased (Guo et al. 2014; Hou et al. 2014a, b; Zou et al. 2016a). Otherwise, when diversion and/or termination occurs, the HF height and the SRV are limited (Li et al. 2016; Zou et al. 2017). Therefore, understanding the influence of BPs on the fracture network generation in a layered formation is significant. To investigate the complicated growth behavior and geometry of HFs, many techniques have been employed in laboratory experiments (e.g., ultrasonic velocity measurements, computerized tomography (CT) scanning, and AE monitoring) (Stanchits et al. 2012, 2015; Hampton et al. 2013; Heng et al. 2014; Hou et al. 2015; Zou et al. 2016a; Li et al. 2017). As a high-frequency analog of induced microseismicity in the field, AE monitoring has increasingly been used to investigate the growth behavior and geometry of HFs (Lockner and Byerlee 1977; Stanchits et al. 2006, 2009; Hampton et al. 2013). Stanchits et al. (2012) investigated the process of HF initiation and propagation in sandstone containing an artificial interface. Then, the influence of fracturing fluid viscosity on the breakdown pressure and propagation speed of HFs in shale was further analyzed (Stanchits et al. 2015). Heng

et al. (2014) monitored the formation of fracture networks in shale formations. Hou et al. (2015) studied the characteristics of injection pressure and AE activity during the formation of fracture networks. However, the application of AE monitoring in laboratory fracturing experiments has mainly been focused on discerning the spatial distribution of internal fractures. Investigations about the failure modes of fracture networks remain scarce. Additionally, the complexity of HF geometries can be obviously varied in layered formations because of the influence of BPs. On the one hand, BPs may increase the complexity of the fracture geometry; on the other hand, BPs may limit the HF height growth (Li et al. 2016; Zou et al. 2016b, 2017). Therefore, understanding the characteristics of injection pressure and AE response associated with different HF geometries is conducive to evaluating HF complexity.

In the current study, to investigate the HF growth and AE response in a layered formation, a series of laboratory hydraulic fracturing experiments was performed on shale specimens using a true triaxial fracturing simulation system. The AE monitoring technique was applied to record the AE activity induced by rock failure throughout the experiments. Spatial distribution and hypocenter mechanisms of AE events were determined by data post-processing. After fracturing, accurate internal complex fracture geometries were observed by CT scanning technique and specimen splitting. Injection pressure curves and AE response during fracturing were analyzed to reveal the HF growth behavior and complexity in the layered formation. Moreover, to investigate the possibility of increasing the fracture complexity, additional experiments were conducted to study the effects of variable injection rates and plugging the open-hole section. The results obtained through these investigations will provide instructional significance for hydraulic fracturing treatments as well as the evaluation of the SRV in layered formations.

2 Experimental Method

2.1 Experimental Equipment and Specimen Preparation

Natural shale blocks were mined from the outcrop of the Long Maxi shale formation, Sichuan Basin, China. Several cores were drilled in directions parallel and perpendicular to the BPs to characterize petrophysical properties of the shale formation. Table 1 lists the results of mineral composition, permeability, and mechanical parameters. Notably, the shale used in this study showed pronounced anisotropic permeability and mechanical parameters. Specifically, the permeability was as low as 10^{-19} m^2 perpendicular to the BPs, whereas in the range of 10^{-19}–10^{-10} m^2 parallel to the BPs.

Table 1 Results of mineral composition, permeability, and mechanical properties

Parameter	Units	Value	Parameter	Units	Value
Quartz content	%	50.6	v	Decimal	0.241/0.236
Carbonate content	%	9.8	T	MPa	6.7/0–2.4
Clay content	%	33.4	σ_c	MPa	284.1/300.9
Feldspar content	%	6.2	k_h	m^2	10^{-19}–10^{-10}
E	MPa	37,200/36,400	k_v	m^2	10^{-19}

Mechanical properties parallel/perpendicular to the BPs

After that, seven cubic specimens (30 cm × 30 cm × 30 cm) were prepared. To simulate the hydraulic fracturing treatment in horizontal well, a 1.6-cm central hole with a depth of 16.5 cm was drilled parallel to the BP. Further, a 13.5-cm wellbore (a steel tube) with internal and external diameters of 0.8 and 1.5 cm, respectively, was glued into the hole, leaving a 3-cm open-hole section in which the HF was initiated (Guo et al. 2014; Zou et al. 2016a). Laboratory experiments were conducted using a true triaxial fracturing simulation system (Ma et al. 2017b), as shown in Fig. 1a.

2.2 Experimental Procedure

The specimens were placed in a core chamber with the BPs parallel to the XY-plane. Triaxial stresses were independently applied by a fracturing simulation system to simulate underground stress conditions and horizontal well completion. Vertical stress (σ_v) was applied perpendicular to the BP, the horizontal minimum (σ_h) and maximum (σ_H) principal stresses were loaded along and perpendicular to the wellbore, respectively, as shown in Fig. 1b. Low-viscosity slickwater ($\mu = 2.5$ mPa s), which is widely used in unconventional reservoirs, was injected into the wellbore during fracturing. Tracer agent was added into the fluid to easily detect hydraulically activated and connected fractures. A 16-channel AE monitoring system (Fig. 1a) was utilized throughout the experiments to reveal the hydraulic fracturing

process and the spatial distribution of the internal fracture network.

In general, when rock failure occurs, two polarity types of the P-wave first motions may be detected by the AE sensors, called dilatational and compressive first motions. The ratio of these two types of first motions varies depending on the failure modes/hypocenter mechanisms (Sato et al. 1990; Lei et al. 1992, 2001; Meglis et al. 1995; Ma et al. 2017a). Compressive first motion tends to dominate when tensile failure occurs, whereas dilatational first motion tends to dominate when a fracture closes; these two types of first motions are approximately detected equally when shear failure occurs. Therefore, investigating the statistical characteristics of the first motions is helpful for determining the failure modes/hypocenter mechanisms. In the current study, the failure modes/hypocenter mechanisms of AE events were statistically estimated according to the proportion of dilatational first motions (λ) for all well-identified polarities. We assigned $\lambda < 0.3$, $0.3 \leq \lambda \leq 0.7$, and $\lambda > 0.7$ to the tensile, shear, and compressive events, respectively (Lei et al. 1992, 2001). To maintain acceptable reliability, only data accepted by more than ten sensors were used to analyze the spatial distribution and the hypocenter mechanism of AE events. After the experiments, the internal fracture geometry was observed by an energetic, industrial CT scanning technique and specimen splitting. The influence of vertical stress and injection rate on HF growth in a layered formation
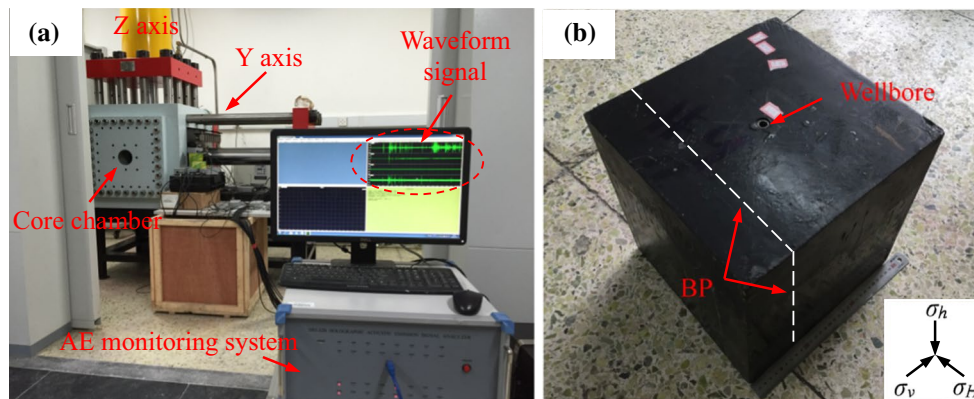

Fig. 1 **a** AE monitoring during laboratory experiments; **b** shale specimen (30 cm × 30 cm × 30 cm)

was analyzed. Moreover, two additional experiments were conducted to investigate the potential of increasing the HF complexity. In Specimen 6, the injection rate was varied during fracturing according to the pressure response. In Specimen 7, the plugging agent was used in the open-hole section to reduce fluid leak-off into the high-permeability BPs. The experimental conditions for each specimen are listed in Table 2.

2.3 Experimental Results

2.3.1 Effect of Vertical Stress

In this section, the influences of σ_v on the fracture geometry were examined. Figure 2 shows the resulting fracture

Table 2 Experimental conditions

Specimen	Stress state (MPa)			Q (mL/min)	μ (mPa s)
	σ_v	σ_h	σ_H		
1	30	10	15	20	2.5
2	25	10	15	20	2.5
3	20	10	15	20	2.5
4	15	10	15	20	2.5
5	15	10	15	5	2.5
6	25	10	15	5–50	2.5
7	20	10	15	20	2.5

geometries of Specimen 1 under a high σ_v of 30 MPa. Two HF branches were initiated from the open-hole section due to the strong heterogeneity of the shale formation (Fig. 2c, f). The HFs extended upward to the boundary of the specimen and downward to BP5, where they terminated (Fig. 2a, f). The BPs were inferred to be effectively compacted under the vertical stress of 30 MPa, which was conducive to the full extension of the HF height. In addition, the HFs tended to penetrate through and then activate the well-cemented BPs (Fig. 2b, e), whereas they diverted along the high-permeability BPs (Fig. 2f). Remarkably, BP6, a high-permeability BP on the bottom of the specimen, was not connected.

Figure 3a, b shows the spatial distribution and hypocenter mechanism of the AE events observed from different perspectives. The three types of hypocenter mechanisms are distinguished by color: the black, red, and blue dots represent the compressive, shear, and tensile events, respectively. As shown in Fig. 3a, shear events tended to dominate the hypocenter mechanisms due to the strong heterogeneity and the existence of weak interfaces (Hampton et al. 2013); these were consecutively numerically followed by tensile and compressive events. Most of the AE events were located in the upper part of Specimen 1, and the events were significantly dense in the open-hole section where the HF was initiated (Figs. 2c and 3a). Therefore, the spatial distribution of AE events can be useful to understand HF initiation and the growth of fracture networks (Stanchits et al. 2012, 2015; Hampton et al. 2013).
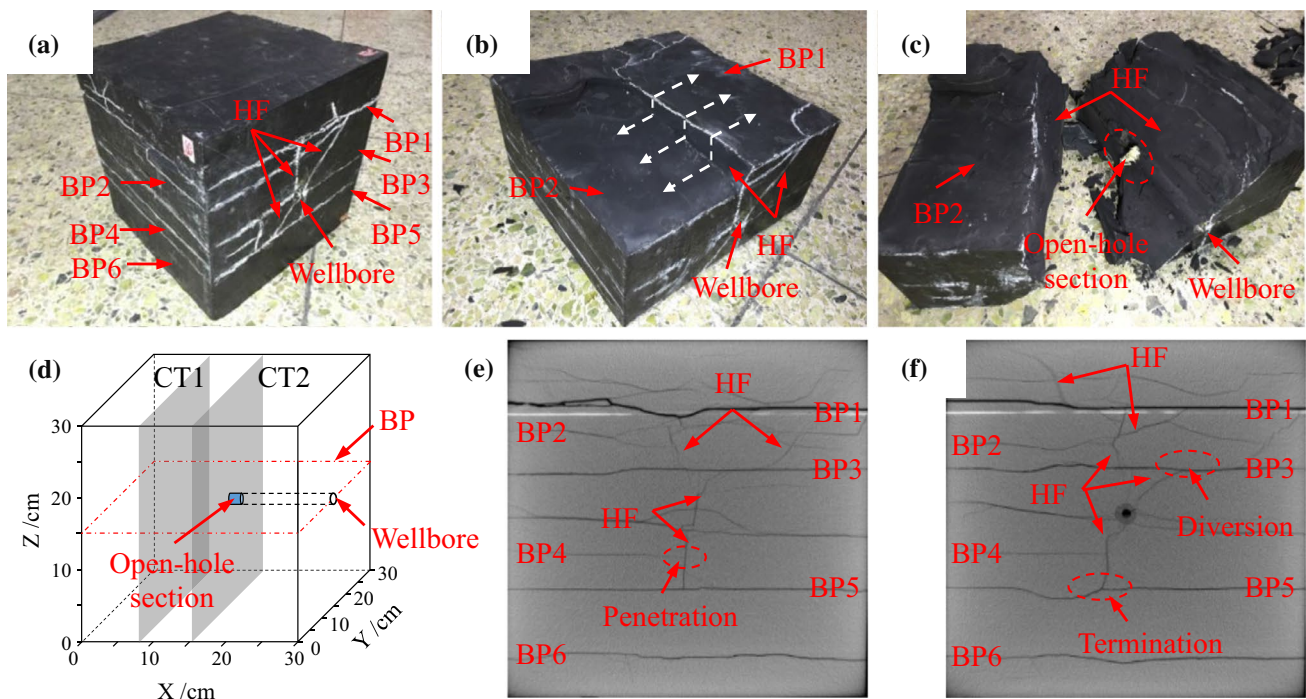

Fig. 2 Fracture geometry of Specimen 1 observed by splitting and CT scanning images

Fig. 3 Specimen 1 **a** 3D spatial location of AE events; **b** side view of the location of the AE events along the wellbore; **c** injection pressure curve and recorded AE activity
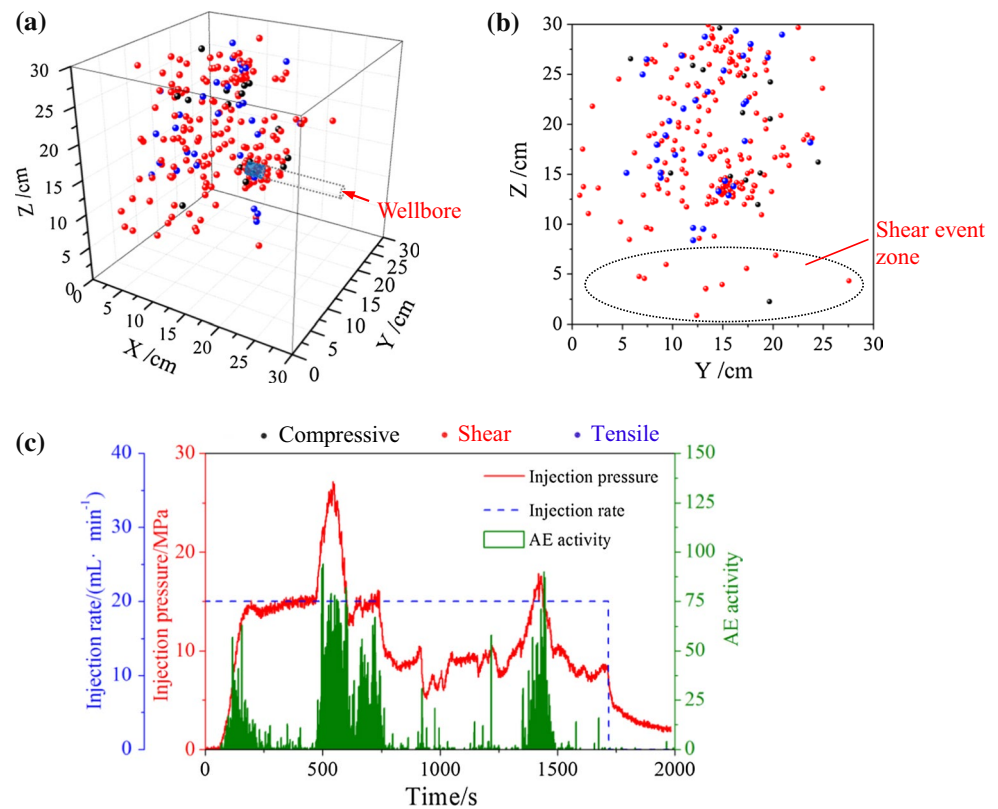

Figure 3c shows the injection pressure and AE activity as functions of injection time (t) during the fracturing. When $t = 50$–200 s, the injection pressure linearly increased and AE activities were simultaneously monitored, as the fluid was injected into the wellbore. Thereafter, the pressure dropped slightly and subsequently remained stable at approximately 15 MPa, which indicated that the BP near the wellbore was dilated and allowed the fracturing fluid to slowly leak into it. In addition, the AE activity weakened when the pressure was stable (in the approximate range of $t = 200$–470 s). The injection pressure surged again once the microfracture was filled with fluid and finally reached a breakdown pressure of 27.2 MPa at $t = 550$ s. Intense AE activity (as high as 100 s^{-1}) lasting for approximately 130 s ($t = 470$–600 s) was clearly detected when the breakdown occurred (Fig. 3c). A complex fracture network was generated in the range of $t = 600$–1500 s, and it was characterized by frequent fluctuations in the injection pressure curve caused by the sequential activation of BPs and NFs (Zhou et al. 2008; Hou et al. 2015), as shown in Fig. 2e, f. In general, the AE activity agreed well with the pressure fluctuation over time (Fig. 3c). Based on the comparison of the CT scanning images (Fig. 2e, f) with the spatial distribution of the AE events (Fig. 3a, b), shear and tensile events were confirmed to be induced in the hydraulically connected region (the upper part of BP5 in Fig. 2f), whereas a shear

event zone was also induced around BP6 (Fig. 3b), which was not connected with the HF network.

Specimen 4 was hydraulically fractured under a lower σ_v of 15 MPa (Table 2), and the internal HF geometry is shown in Fig. 4. Similar to Specimen 1, two HF branches were initiated from the open-hole section and reoriented along the wellbore becoming perpendicular to the direction in which σ_h was applied (Fig. 4b, c). The HF branches finally merged away from the wellbore as shown in Fig. 4c, e. The CT scanning image (Fig. 4f) shows that the hydraulically connected region was confined between BP1 and BP3 in Specimen 4. Furthermore, BP1 was not dyed by the tracer agent, indicating that the HF terminated and did not activate BP1. Figure 4e shows that another high-permeability BP, namely BP4, was not connected with the HF.

Considering the fact that none of the high-permeability BPs were directly connected with the wellbore in Specimen 4 (Fig. 4a, f), the injection pressure increased linearly and reached a breakdown pressure of 20.8 MPa at $t = 100$ s (Fig. 5c) during which intense AE activity (> 250 s^{-1}) occurred and massive shear and tensile events were induced near the open-hole section (Fig. 5a, b) as the HF was initiated. Thereafter, the HF rapidly extended toward the boundary of Specimen 4 without significant influence from BPs or NFs (Fig. 4e, f). Consequently, the injection pressure was relatively steady around 10 MPa following the HF initiation until the injection was stopped (Fig. 5c). Few AE events
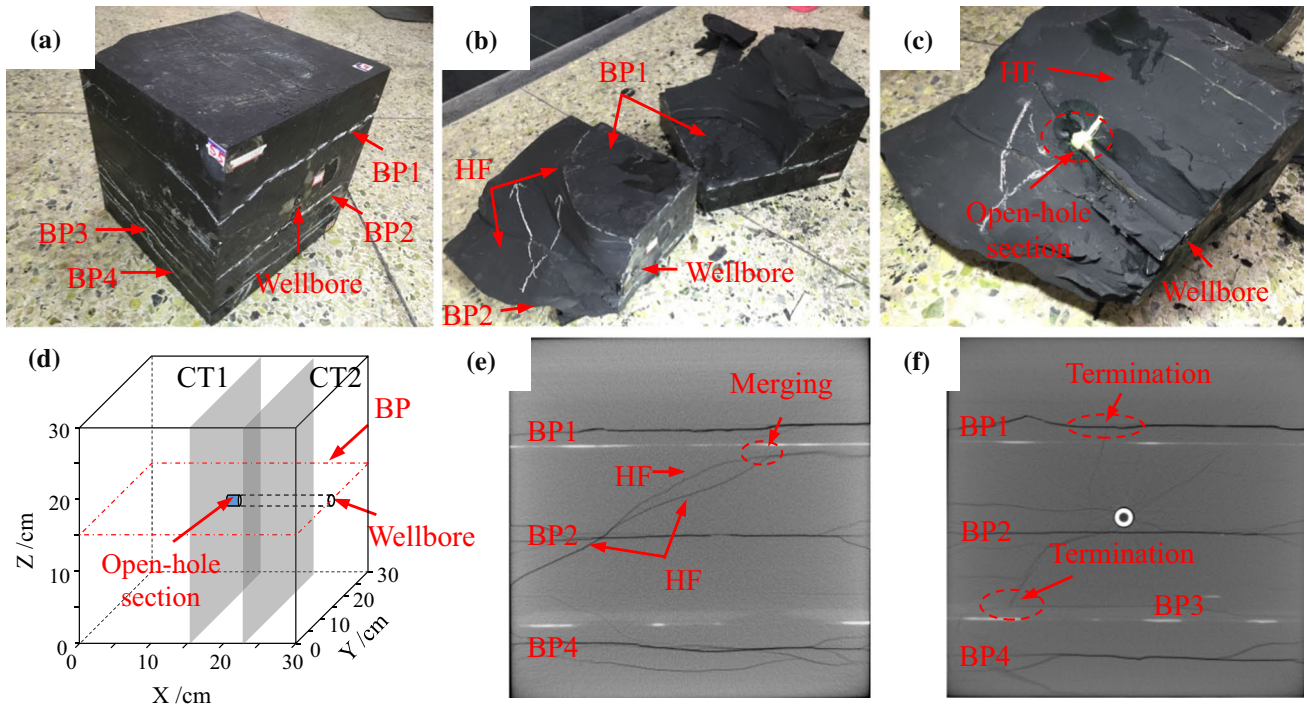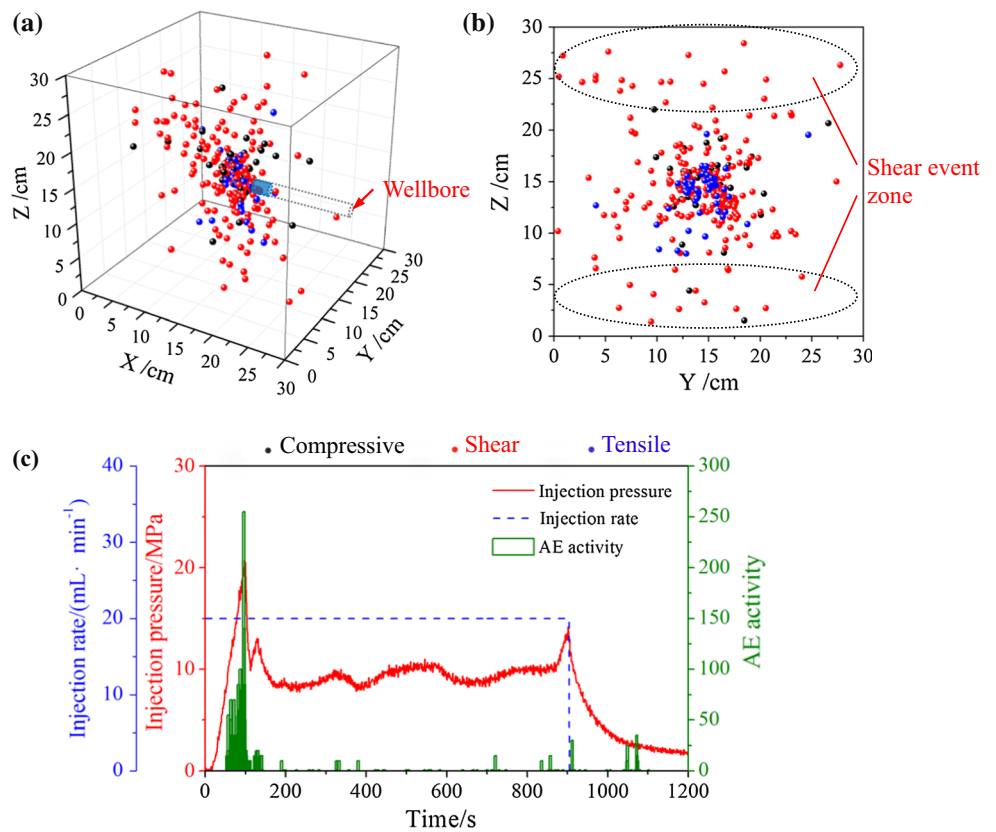
Fig. 4 Fracture geometry of Specimen 4 observed by splitting and CT scanning images

Fig. 5 Specimen 4 **a** 3D spatial location of AE events; **b** side view of the location of the AE events along the wellbore; **c** injection pressure curve and recorded AE activity

were induced when the fracturing fluid flowed through the HF ($t = 200$–900 s). Although the fracture geometry of Specimen 4 was much simpler than that of Specimen 1 (Figs. 2f and 4f), the AE events in Specimen 4 were similarly dispersed due to the wrapped HF surfaces, as shown in Figs. 4b and 5a. In addition, when Figs. 4e and 5b were compared, three types of AE events were located in the region between BP1 and BP3, but no tensile events were induced in either the top or the bottom of Specimen 4.

2.3.2 Effect of Injection Rate

To investigate the effect of injection rate, Specimen 5 was hydraulically fractured under the same stress conditions as Specimen 4 but with a lower injection rate of 5 mL/min. Before the experiment, a high-permeability bedding zone was observed near the wellbore (Fig. 6a, d). Consequently, the HF was initiated and subsequently propagated along the tortuous BPs under the lower injection rate when it encountered the weak bedding zone (Fig. 6b). Figure 7c shows the injection pressure and AE activity recorded during the experiment. The injection pressure initially increased rapidly and linearly until $t = 100$ s, and then began to deviate from the straight line and increased in a fluctuating manner ($t = 100$–160 s). This behavior indicated that the fracturing fluid was slowly leaking into the high-permeability bedding zone as the injection pressure increased. Finally, the injection pressure attained a breakdown pressure of 14.3 MPa, which was lower than the breakdown pressures of Specimens 1 and 4, and then sharply decreased to approximately 1 MPa (Fig. 7c). An extremely high rate of AE (840 s^{-1}) was detected at the precise moment of the breakdown. This was most likely caused by the perturbation of multiple

high-permeability BPs. The spatial distribution of the AE events (Fig. 6d) aligned closely with the location of the high-permeability bedding zone (Fig. 7b). Few AE events were detected around the open-hole section of Specimen 5 (Fig. 7a, b) because of the low breakdown pressure; remarkably, a small number of shear events were scattered around the local position of BP1 (Fig. 7b), which tended to be relatively unstable because of interface tortuosity (Fig. 6d). After reaching the boundaries, the low-viscosity fracturing fluid was able to infiltrate back into the specimen along the NFs or BPs (Fig. 6d) and induce scattered AE events near the surface, as shown in Fig. 7b.

2.3.3 Effect of Variable Injection Rate and Plugging Inside the Open-Hole Section

Previous studies have suggested that BPs play a significant role in the generation of three-dimensional complex fracture networks (Hou et al. 2014b; Zou et al. 2016b). However, in the current study, the HF height growth tended to be limited by high-permeability BPs (see Specimen 5). Further, a BP-dominated fracture geometry significantly decreases SRV (Hou et al. 2014a; Zou et al. 2016a). Therefore, ensuring the initiation and full extension of HF height in layered formations is important. Prior to the experiments, high-permeability BPs were observed near the wellbore in Specimens 6 (see BP3 in Fig. 8) and 7 (BP3 in Fig. 10). To investigate potential techniques to increase fracture complexity, variable injection rate was used in Specimen 6 and plugging agent was applied inside the open-hole section of Specimen 7.

Specimen 6 was hydraulically fractured under a vertical stress of 25 MPa (Table 2). The injection rate was artificially altered according to the pressure response during

Fig. 6 Fracture geometry of Specimen 5 observed by splitting and CT scanning images
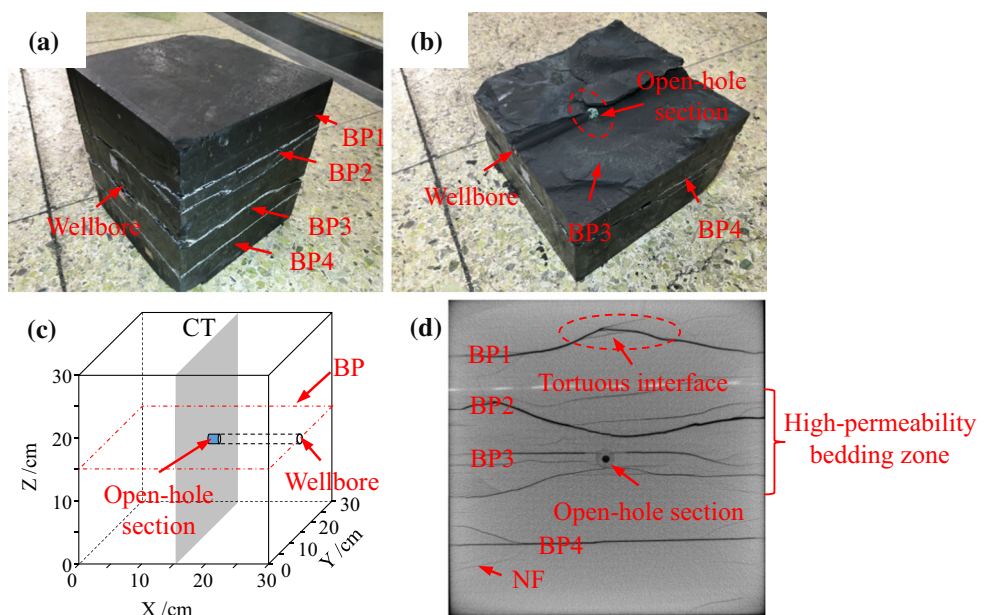
Fig. 7 Specimen 5 **a** 3D spatial location of AE events; **b** side view of the location of the AE events along the wellbore; **c** injection pressure curve and recorded AE activity
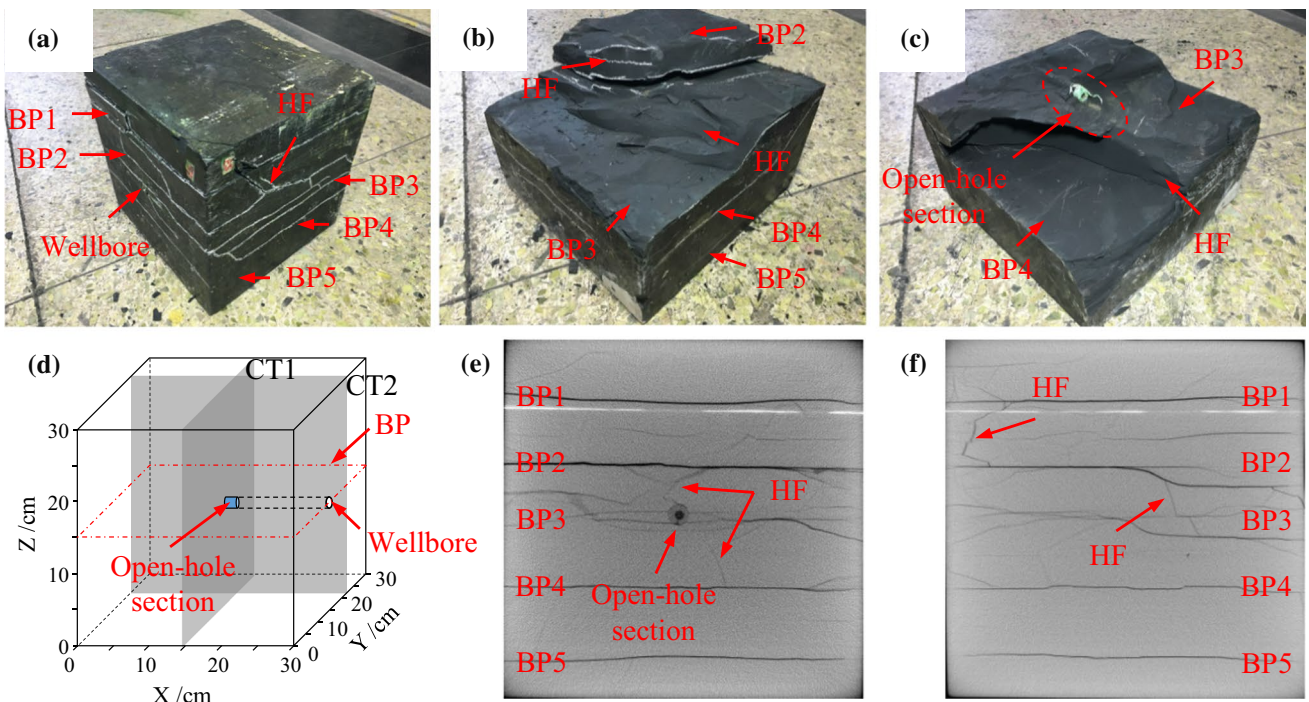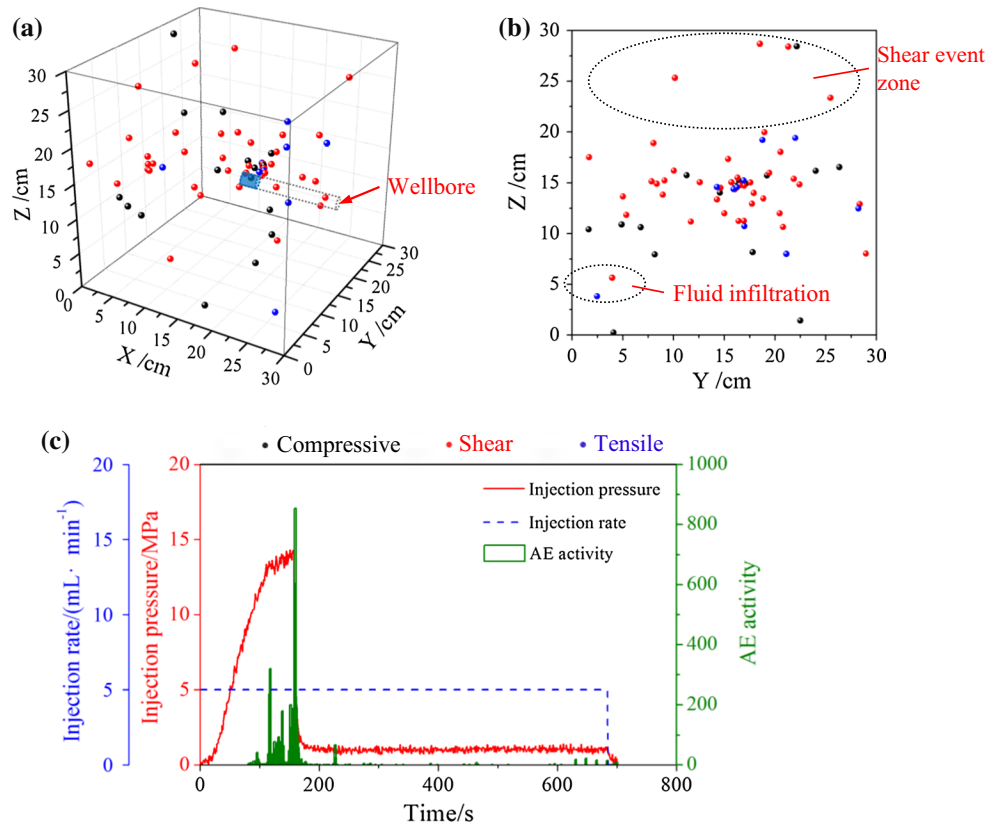

Fig. 8 Fracture geometry of Specimen 6 observed by splitting and CT scanning images

the experiment. Figure 9 shows the details of the injection scheme. The fracturing process was divided into three pumping stages by twice shut-in operations (see the blue dash line in Fig. 9). In the first stage (t = 0–1860 s), the open-hole section was initially pressurized with a low injection rate of 5 mL/min. At t = 300 s, the pressure began to decrease from approximately 5.0–3.0 MPa, indicating that the weak BP3 near the wellbore (Fig. 8e) was dilated and the fracturing fluid leaked into it. Then, the injection rate was increased to 10 mL/min at t = 360 s and remained constant for approximately 5 min, after which the injection pressure gradually increased to about 6.5 MPa and then remained constant once again. Meanwhile, weak AE activities were detected, as shown in Fig. 9c. When the injection rate was increased to 20 mL/min at t = 690 s, the pressure started to significantly increase and the AE activities intensified. Specimen 6 was ultimately fractured at a breakdown pressure of 19.5 MPa at approximately t = 910 s and was accompanied by intense AE activity (75 s^{-1}), as shown in Fig. 9c. This indicated that a hydraulically induced fracture was created in Specimen 6

at this moment. Frequent pressure fluctuations and multiple periods of intense AE activities were then simultaneously observed in the range of t = 960–1100 s, as was seen in Specimen 1 (compare Figs. 3c and 9c). When the pressure tended to be stable, the injection pump was shut-in until the pressure decreased to nearly 0 MPa to ensure that the HF was closed. The injection pump was then restarted at a constant injection rate of 20 mL/min for the second stage (t = 2010–2280 s in Fig. 9c) during which the pressure quickly increased and reached a value approximately equal to the initial shut-in pressure. Figure 9c also indicates that no evident AE activity was monitored during the second injection period in Specimen 6, suggesting that the existing HF was reopened and no new HFs were initiated. The injection pump was then shut-in again. During the third pumping stage (t = 2420–2620 s in Fig. 9c), a higher injection rate of 50 mL/min was used to increase the HF complexity as much as possible. Figure 9c shows two breakdown pressures, 15.7 and 16.7 MPa, which were evident in the injection pressure curve. In addition, drastic AE activities were monitored
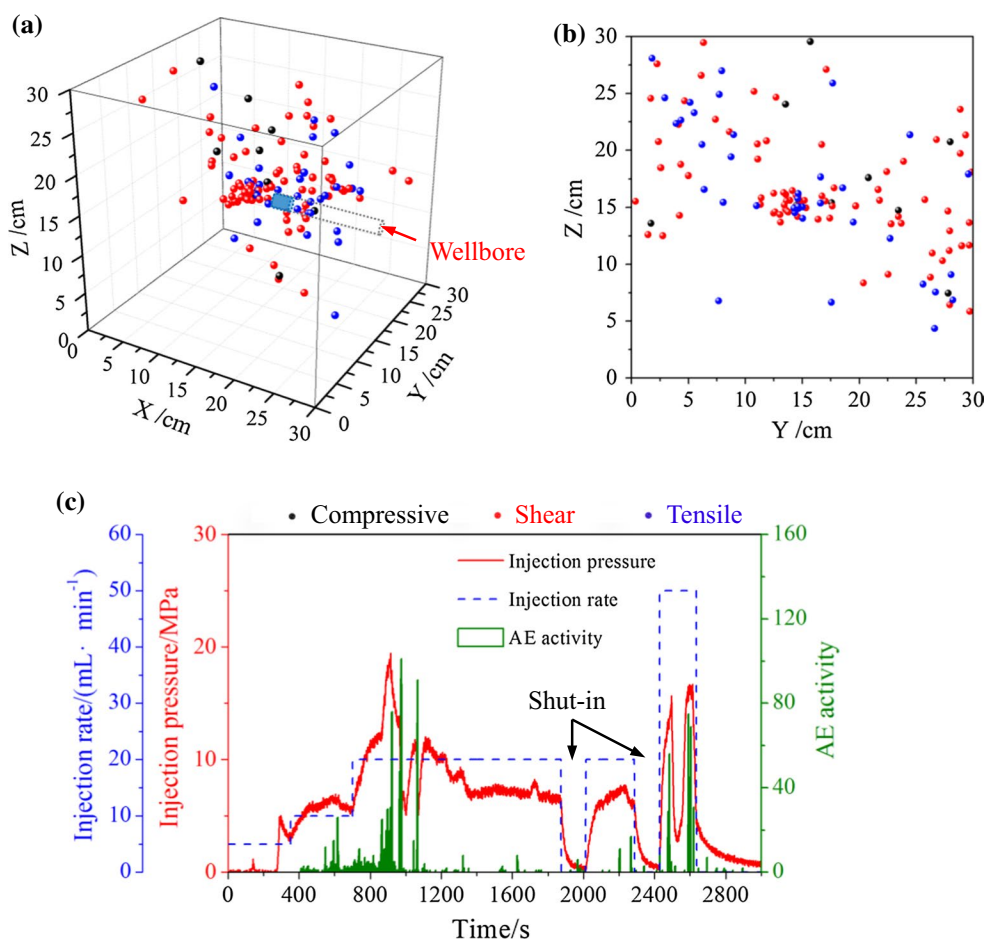

Fig. 9 Specimen 6 **a** 3D spatial location of AE events; **b** side view of the location of the AE events along the wellbore; **c** injection pressure curve and recorded AE activity

during $t = 2420$–2500 s and $t = 2600$–2620 s. Therefore, it can be concluded that new HFs were induced by increasing the injection rate. The CT scanning image (Fig. 8e) and the specimen splitting (Fig. 8c) demonstrate that one HF was successfully initiated and propagated upward and downward even though BP3 was connected with the open-hole section. In the upper part of Specimen 6, the HF encountered and diverted along BP2, and a new HF was then re-initiated on the opposite side of the BP2 interface (Fig. 8e, f). The spatial distribution of the AE events also indicated the generation of a complex fracture network in the upper side of the specimen, as shown in Fig. 9a, b.

Plugging agents are widely used for filtration reduction and fracture reorientation in the laboratory and on the field (Zhou et al. 2009; Wang et al. 2015). In the current study, to prevent fluid leak-off into the BPs near the wellbore, in Specimen 7, fibers were placed in the open-hole section to plug the high-permeability BPs. A vertical stress of 20 MPa was applied, and the injection rate was maintained at 20 mL/min, while the injection pressure and the AE activity were recorded (Fig. 11). The data shown in Fig. 11c demonstrate that the injection pressure rapidly and linearly increased and reached approximately 50.0 MPa in about 170 s. The constant pressure build-up rate and the abnormally high-pressure value (Fig. 11c) indicated that the weak BP3 (Fig. 10e) was effectively plugged by the fibers and the influence of fluid leak-off was negligible. Thereafter, microfracture was induced near the wellbore ($t = 210$ s in Fig. 11c) and resulted

in a slight decrease in the injection pressure. At $t = 300$ s, the pressure curve markedly decreased from the breakdown pressure of 48.2 to nearly 2 MPa. Figure 10 shows that the HF was initiated and grew in the vertical direction (Fig. 10b, e) rather than along BP3, which was connected with the open-hole section. On account of the high breakdown pressure, the HF extended rapidly to the boundary of the specimen and resulted in a sharp pressure drop in the injection curve. Although the fracture geometry was relatively simple, drastic AE activity was detected at $t = 200$–300 s (Fig. 11c) and numerous AE events were located near the open-hole section. This high intensity of AE activity was explained by the quick release of a large amount of energy that had accumulated in the open-hole section because of the high injection pressure.

3 Discussion

The experimental results show that high-permeability BPs played an important role in HF geometry, especially the growth of HF height. Various HF geometries created in layered specimens could be obviously distinguished by the injection pressure curve and AE response. Table 3 provides a summary of the experimental results for each of the seven specimens. Figure 12a depicts the geometrical information of the internal fractures (i.e., initial weak BPs observed before the experiments and ultimate fracture geometries
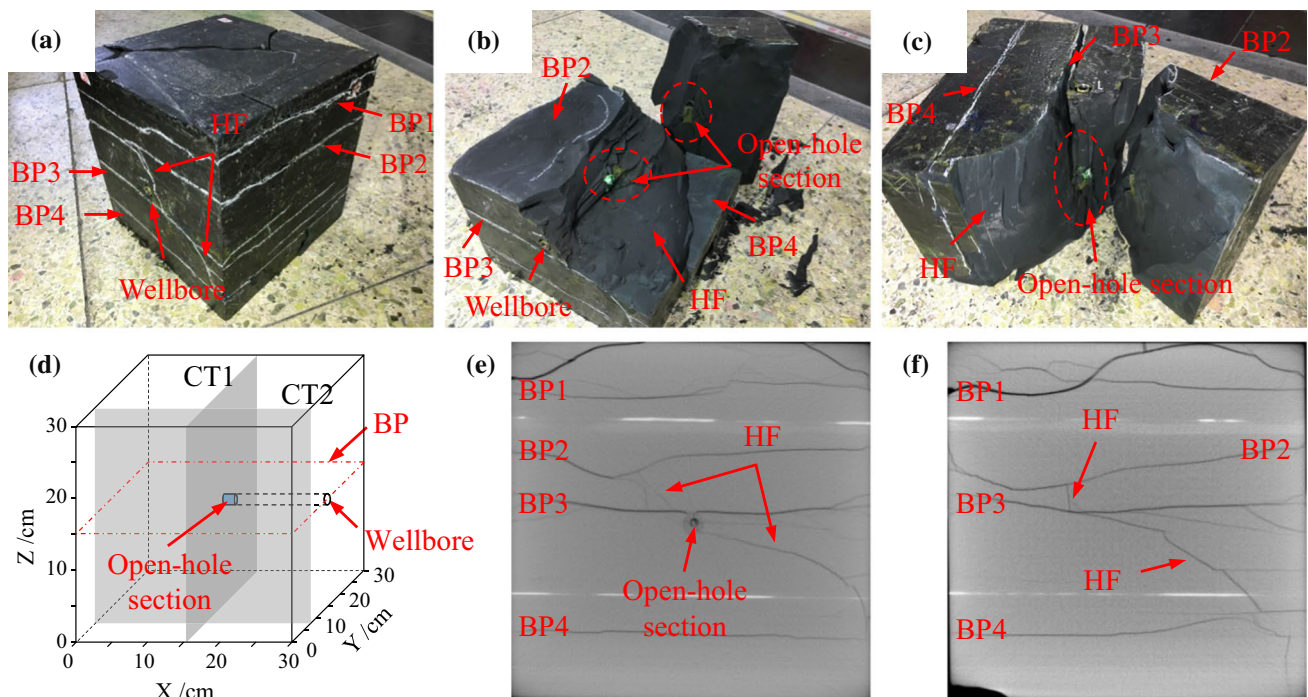

Fig. 10 Fracture geometry of Specimen 7 observed by splitting and CT scanning images

Fig. 11 Specimen 7 **a** 3D spatial location of AE events; **b** side view of the location of the AE events along wellbore; **c** injection pressure curve and recorded AE
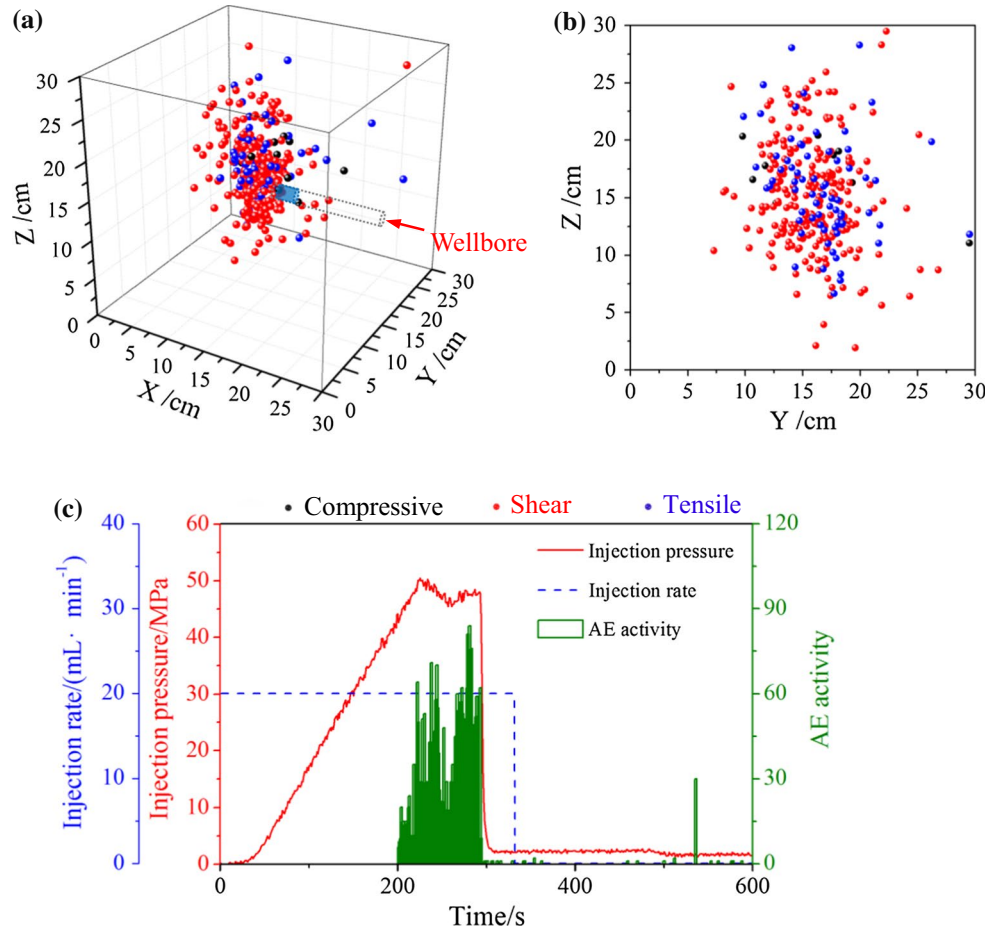

Table 3 Summary of experimental results for all specimens

Specimen	Fracture characterization	Injection pressure response		N_{AE}
		p_b (MPa)	Post-breakdown pressure	
1	Complex fracture network (Fig. 2)	27.2	Frequently fluctuated between 5 MPa and 18 MPa	230
2	BP-dominated fracture	4.5	Sharply dropped to 0 MPa	4
3	BP-dominated fracture	6.9	Sharply dropped to 0 MPa	7
4	Two HF branches (Fig. 4)	20.8	Stabilized at about 10 MPa	360
5	BP-dominated fracture (Fig. 6)	14.3	Sharply dropped to 1 MPa	66
6	Fracture network (Fig. 8)	19.5 (1st pumping stage) 15.7, 16.7 (3rd pumping stage)	Fluctuated and then stabilized at approximately 7.2 MPa	129
7	HF (Fig. 10)	48.2	Sharply dropped to 2 MPa	313

after the experiments) in five specimens. Comparing the HF geometry results, a complex fracture network was created when the HF penetrated through and opened multiple BPs, as in Specimens 1 (Fig. 2) and 6 (Fig. 8). This observation agreed well with the experimental results reported by Guo et al. (2014), Heng et al. (2014), and Zou et al. (2016a). In this case, frequent pressure fluctuations and multiple, intense

AE activities occurred simultaneously ($t = 600$–1500 s in Fig. 3c and $t = 960$–1100 s in Fig. 9c), which is consistent with the findings reported by Hou et al. (2015). When HF height growth was limited by a high-permeability BP (like BP3 in Specimen 4), the injection pressure was relatively steady. No intense AE activity was induced because fluid leak-off dominated (Fig. 5c). Remarkably, when a
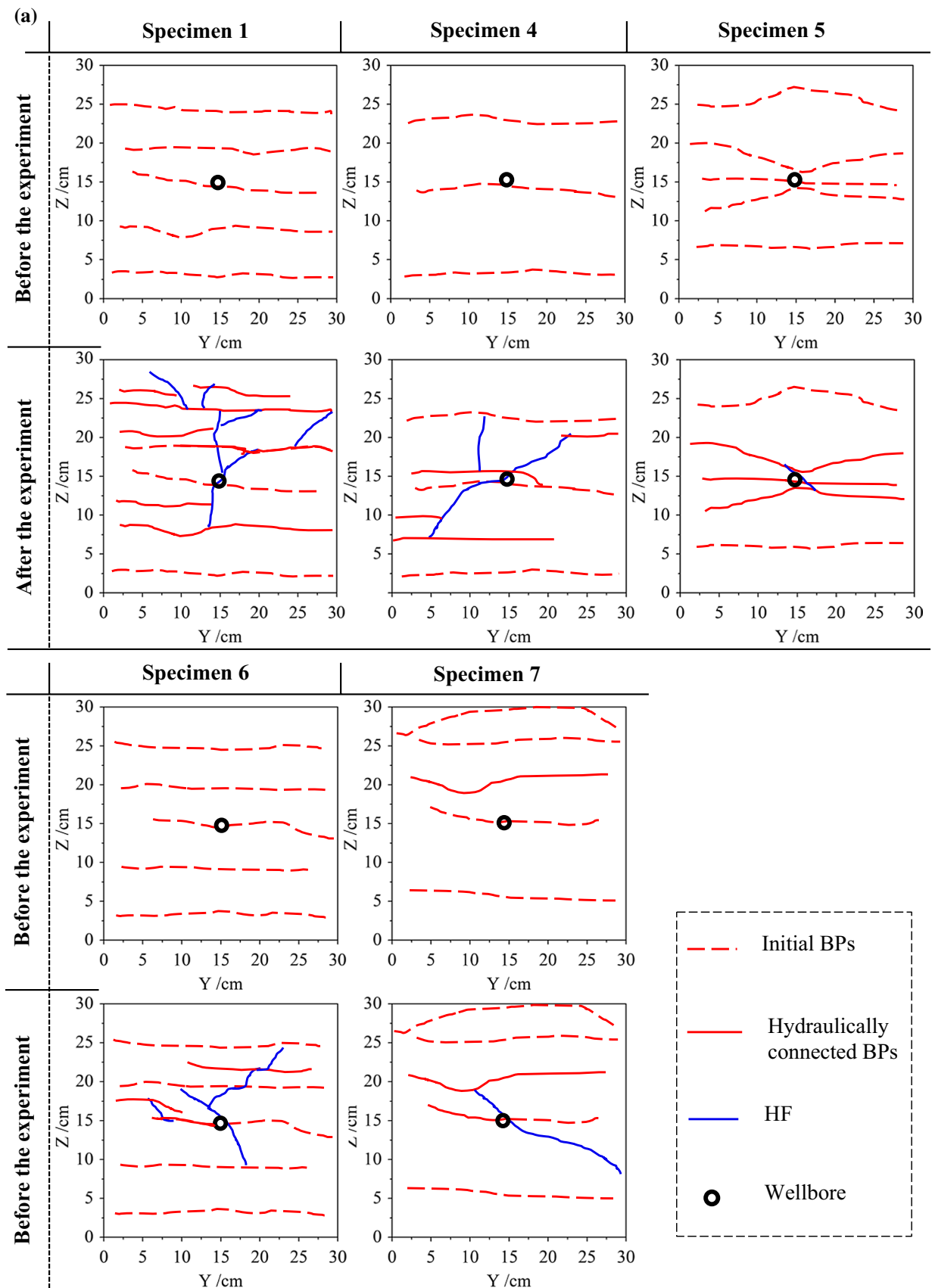
Fig. 12 **a** Geometries of the internal fractures before and after experiments; **b** statistical results of the hypocenter mechanism for all specimens
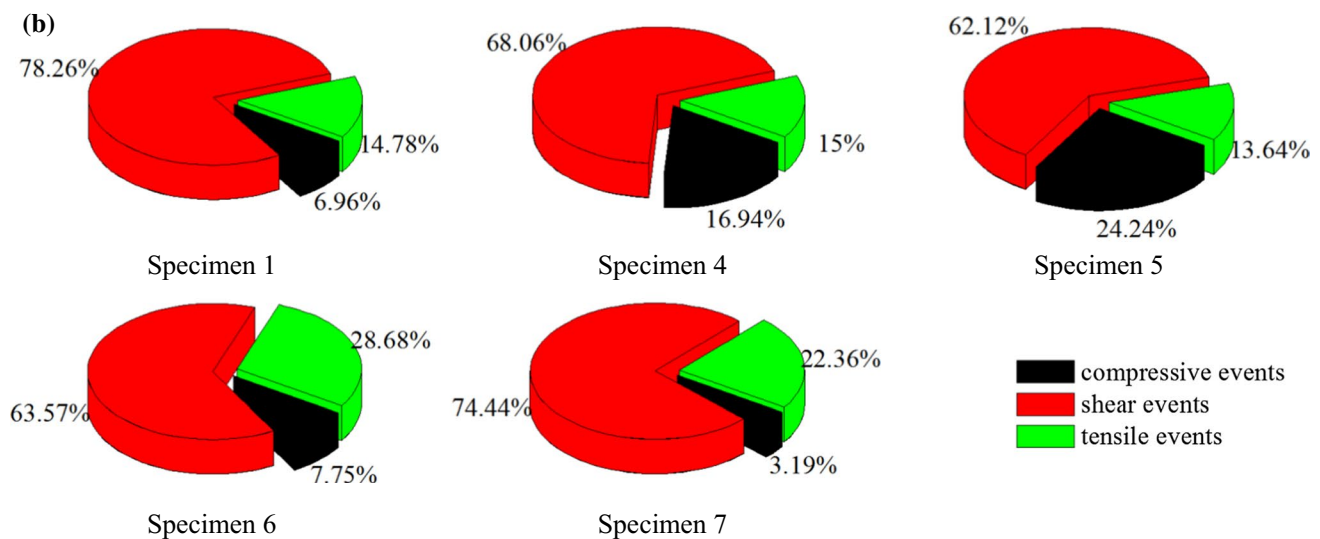
(b)

Fig. 12 (continued)

high-permeability BP was connected to the open-hole section, the HF was more likely to initiate along this BP, which resulted in a BP-dominated fracture geometry, such as that observed in Specimen 5 (Fig. 6b, d). Once the simple fracture geometry was created, the breakdown pressure tended to be followed by a sharp decrease in the injection pressure curve, as shown in Fig. 7c. Additionally, the spatial distribution of the AE events clearly depicted that the hydraulically connected region was limited (Fig. 7a, b).

Varying the injection rate and plugging inside the open-hole section were both demonstrated to be feasible techniques to increase the HF height growth and the fracture complexity in the layered formation with multiple high-permeability BPs. The high injection rate reduced the influence of fluid leak-off and increased the pressure build-up rate. Furthermore, varying the injection rate led to pressure pulses, which facilitated the penetration of the HFs through the weak BPs (Hou et al. 2014a; Zou et al. 2016a). Consequently, both the HF height growth and the geometric complexity were successfully increased, as indicated by the CT scanning images (Fig. 8e, f) and the AE monitoring results (Fig. 9b). In addition, plugging inside the open-hole section effectively reduced fluid infiltration into the high-permeability BPs that connected with the wellbore, which is beneficial to the initiation of the HFs and prevents the generation of BP-dominated fracture geometries (see Figs. 10, 11a, b). Considering that extremely high breakdown pressure (Fig. 11c) leads to difficulties in the hydraulic fracturing treatment (Wang et al. 2015), the quantity of the plugging agent used should be optimized through further studies.

The analysis of the experimental results suggests that it is feasible to qualitatively evaluate the complexity of HF geometry based on the combined characteristics of

an injection pressure curve and AE response. However, quantitatively calculating the SRV is more important for predicting the productivity of oil and gas fields. Mayerhofer et al. (2010) suggested that the size of the SRV could be calculated according to the 3D spatial distribution of the AE/microseismic event cloud. However, in the current study, there were obvious differences between the spatial distribution of AE events and the internal fracture geometries observed in the CT scanning images (Specimens 1, 4, and 5). The AE events were induced not only within the hydraulically connected region but also around some BPs that were not hydraulically connected. King et al. (2008) suggested that only fractures that are hydraulically connected with HFs can be regarded as the effective SRV because of the ultra-low permeability of the matrix in unconventional reservoirs. Therefore, we can conclude that the HF height growth and/or the SRV in a layered formation might be overestimated if based on the spatial distribution of microseismic/AE events. Therefore, to understand the relationship between the effective SRV (i.e., the hydraulically connected region) and the localization of AE events, hypocenter mechanisms were further discussed to determine the failure modes of the fractures. Figure 12b shows the statistical results of three types of AE events for each specimen. Shear failure tended to dominate because of the heterogeneity of the specimens and the existence of geological discontinuities (Hampton et al. 2013). In five specimens, the percentage of shear events exceeded 60% and was particularly high in Specimen 1, where a complex fracture was created (Fig. 12b). This indicates that shear failure dominates during the generation of fracture networks in shale formations (Zhou et al. 2008; Zou et al. 2016b). Remarkably, a

comparison between the CT scanning images and the AE monitoring results showed that shear and tensile events were induced in the hydraulically connected region, whereas shear event zones were located around the BPs that were not hydraulically connected (Figs. 3c, 5c, and 7c) because of the changes in the stress state acting on the BP interfaces. It was well known that additional stress field will be induced surrounding an HF because of the high net pressure within the HF (Warpinski and Branagan 1989). Theoretical studies have shown that this stress perturbation will reduce the normal stress and induce additional shear stress to the BP interfaces ahead of the HF tip. Consequently, shear instability of BPs would tend to occur. This was also numerically determined by Agarwal et al. (2012) and Warpinski et al. (2013). This phenomenon was more common in the laboratory experiments of the current study because of many obviously weak BPs in the specimens (Tables 1 and 2). Therefore, it is recommended that the hypocenter mechanism is taken into account while interpreting the HF geometry and evaluating the effective SRV.

It was also observed that the appearance of a shear event zone was closely related to the cement condition and mechanical properties of the natural BPs. As shown in Table 2, the mechanical strengths of some BPs were significantly low, which is not usually the case with underground rock. Thus, the influence of stress perturbation may have been exaggerated in the current study. It is possible that shear instability can only be clearly observed under certain conditions in the field (Agarwal et al. 2012). Moreover, the polarity analysis (i.e., the statistical analysis of the P-wave first motions) used in this study was a qualitative method based on the hypothesis that there are only two types of pure failure mode, namely shear and tensile failure (Lei et al. 1992, 2001; Meglis et al. 1995; Zang et al. 1998). Experimental and theoretical studies have described a hybrid failure mode called tensile–shear failure (Ramsey and Chester 2004; Zhu 2017). To distinguish pure and hybrid failure modes, spatial relationship between the directions of the displacement discontinuity vector and the normal vector to the fracture surface should be determined (Ohtsu 1991; Baker and Young 1997). In future studies, an alternative method called moment tensor inversion (Ohtsu 1991; Hampton et al. 2013) could be implemented to determine this quantitative information, which could then be used to analyze the fracture growth mechanism.

The generation process of a fracture network is complicated. To obtain a detailed understanding of the dynamic process of a fracture network generation in layered formations, sequential and spatial evolution characteristics of AE events should be considered. Analyses to address this are currently underway.

4 Conclusion

A series of laboratory experiments combining with CT scanning and AE monitoring techniques were conducted to investigate HF growth and AE response in a layered formation. The conclusions are as follows:

1. Fracture complexity was significantly increased when a vertically growing HF could connect with and open more BPs. This intersection between an HF and multiple BPs led to frequent fluctuations in the injection pressure curve and induced intense AE activities. In addition, the generation of a complex fracture network is appropriately reflected by the three-dimensionally distributed AE events.

2. When an HF encountered a high-permeability BP near the wellbore and grew along it, the breakdown pressure tended to be followed by a sharp decrease. Thus, most AE events were induced at breakdown, after which no evident AE activity could be detected. The spatial distribution of the AE events showed that a BP-dominated fracture geometry significantly decreases SRV.

3. Increasing the injection rate was beneficial to reduce the influence of fluid leak-off and increase the pressure build-up rate, which facilitated the penetration of an HF through high-permeability BPs and created a complex fracture network. This was evidently demonstrated by the characteristics of the injection pressure curve and the spatial distribution of AE events. Moreover, plugging inside the open-hole section was demonstrated as another effective way to reduce fluid leak-off into high-permeability BPs. And thus, it was useful to prevent BP-dominated fractures in the layered formation.

4. Analysis of the hypocenter mechanisms suggested that shear and tensile events were induced in the hydraulically connected region. Shear events were also detected around the BPs that were not hydraulically connected, which leads to the overestimation of the HF height growth and/or the SRV in the layered formation based on the spatial distribution of microseismic/AE events.

References

Agarwal K, Mayerhofer M, Warpinski N (2012) Impact of geomechanics on microseismicity. In: SPE European unconventional

resources conference and exhibition, Society of Petroleum Engineers

Baker C, Young RP (1997) Evidence for extensile crack initiation in point source time-dependent moment tensor solutions. Bull Seismol Soc Am 87(6):1442–1453

Beugelsdijk LJL, de Pater CJ, Sato K (2000) Experimental hydraulic fracture propagation in a multi-fractured medium. In: SPE Asia Pacific conference on integrated modeling for asset management, Society of Petroleum Engineers

Casas L, Miskimins JL, Black A, Green S (2006) Laboratory hydraulic fracturing test on a rock with artificial discontinuities. In: SPE annual technical conference and exhibition, Society of Petroleum Engineers

Cipolla CL, Warpinski NR, Mayerhofer MJ, Lolon EP (2008) The relationship between fracture complexity, reservoir properties, and fracture treatment design. SPE Prod Oper 25(4):438–452

Cipolla CL, Mack MG, Maxwell SC, Downie RC (2011) A practical guide to interpreting microseismic measurements. In: North American unconventional gas conference and exhibition, Society of Petroleum Engineers

Fisher MK, Wright CA, Davidson BM, Steinsberger NP, Buckler WS, Goodwin A, Fielder EO (2005) Integrating fracture mapping technologies to improve stimulations in the Barnett shale. SPE Prod Facil 20(2):85–93

Guo TK, Zhang SC, Qu ZQ, Zhou T, Xiao YS, Gao J (2014) Experimental study of hydraulic fracturing for shale by stimulated reservoir volume. Fuel 128(14):373–380

Hampton J, Frash L, Gutierrez M (2013) Investigation of laboratory hydraulic fracture source mechanisms using acoustic emission. In: 47th U.S. rock mechanics/geomechanics symposium, American Rock Mechanics Association

Heng S, Yang CH, Zeng YJ, Guo YT, Wang L, Hou ZK (2014) Experimental study on hydraulic fracture geometry of shale. Chin J Geotech Eng 36(7):1243–1251

Hou B, Chen M, Cheng W, Tan P (2014a) Fracturing mechanism of shale gas reservoir with variable pump rates. Chin J Geotech Eng 36(11):2149–2152

Hou B, Chen M, Li ZM, Wang Y, Diao C (2014b) Propagation area evaluation of hydraulic fracture networks in shale gas reservoirs. Pet Explor Dev 41(6):833–838

Hou B, Chen M, Tan P, Li D (2015) Monitoring of hydraulic fracture network by acoustic emission method in simulated triaxial fracturing system of shale gas reservoirs. J China Univ Pet 39(1):66–71

King GE, Haile L, Jim S, Dobkins TA (2008) Increasing fracture path complexity and controlling downward fracture growth in the Barnett shale. In: SPE gas production conference, Society of Petroleum Engineers

Lei XL, Nishizawa O, Kusunose K, Satoh T (1992) Fractal structure of the hypocenter distributions and focal mechanism solutions of acoustic emission in two granites of different grain sizes. J Phys Earth 40(6):617–634

Lei XL, Kusunose K, Rao MVMS, Nishizawa O, Satoh T (2001) Quasi-static fault growth and cracking in homogeneous brittle rock under triaxial compression using acoustic emission monitoring. J Geophys Res 105(B3):6127–6139

Li H, Zou YS, Valko PP, Economides C (2016) Hydraulic fracture height predictions in laminated shale formations using finite element discrete element method. In: SPE hydraulic fracturing technology conference, Society of Petroleum Engineers

Li N, Zhang SC, Ma XF, Zou YS, Chen M, Li SH, Zhang YN (2017) Experimental study on the propagation mechanism of hydraulic fracture in glutenite formations. Chin J Rock Mech Eng. https://doi.org/10.13722/j.cnki.jrme.2017.0159

Lockner D, Byerlee JD (1977) Hydrofracture in Weber sandstone at high confining pressure and differential stress. J Geophys Res Atmos 82(14):2018–20265

Ma XF, Li N, Yin CB, Li YC, Zou YS, Wu S, He F (2017a) Hydraulic fracture propagation geometry and acoustic emission interpretation: a case study of Silurian Longmaxi Formation shale in Sichuan Basin. Pet Explor Dev. https://doi.org/10.11698/PED.2017.05.00

Ma XF, Zou YS, Li N, Chen M, Zhang YN, Liu ZZ (2017b) Experimental study on the mechanism of hydraulic fracture growth in a glutenite reservoir. J Struct Geol 97:37–47

Maxwell SC, Urbancic TI, Steinsberger N, Zinno R (2002) Microseismic imaging of hydraulic fracture complexity in the Barnett shale. In: SPE annual technical conference and exhibition, Society of Petroleum Engineers

Mayerhofer MJ, Lolon E, Warpinski NR, Cipolla CL, Walser DW, Rightmire CM (2010) What is stimulated reservoir volume? SPE Prod Oper 25(1):89–98

Meglis IL, Chows TM, Young RP (1995) . International Journal of Rock Mechanics & Mining Sciences & Geomechanics Abstracts 32(8):741-750

Meglis IL, Chows TM, Young RP (1995b) Progressive microcrack development in tests in Lac du Bonnet granite—I. Acoustic emission source location and velocity measurements. Int J Rock Mech Min Sci Geomech Abstr 32(8):741–750

Ohtsu M (1991) Simplified moment tensor analysis and unified decomposition of acoustic emission source: application to in situ hydrofracturing test. J Geophys Res Solid Earth 96(B4):6211–6221

Olson J E, Bahorich B, Holder J (2012) Examining hydraulic fracture: natural fracture interaction in hydrostone block experiments. In: SPE hydraulic fracturing technology conference, Society of Petroleum Engineers

Potluri NK, Zhu D, Hill AD (2005) The effect of natural fractures on hydraulic fracture propagation. In: SPE European formation damage conference, Society of Petroleum Engineers

Ramsey JM, Chester FM (2004) Hybrid fracture and the transition from extension fracture to shear fracture. Nature 428(6978):63–66

Renshaw CE, Pollard DD (1995) An experimentally verified criterion for propagation across unbounded frictional interfaces in brittle, linear elastic materials. Int J Rock Mech Min Sci Geomech Abstr 32(3):237–249

Sato T, Nishizawa O, Kusunose K (1990) Fault development in Oshima Granite under triaxial compression inferred from hypocenter distribution and focal mechanism of acoustic emission. Sci Rep Tohoku Univ Fifth 33:241–250

Stanchits S, Vinciguerra S, Dresen G (2006) Ultrasonic velocities, acoustic emission characteristics and crack damage of basalt and granite. Pure appl Geophys 163(5):975–994

Stanchits S, Fortin J, Gueguen Y, Dresen G (2009) Initiation and propagation of compaction bands in dry and wet Bentheim sandstone. Pure appl Geophys 166(5):843–868

Stanchits S, Surdi A, Edelman E, Suarez-Rivera R (2012) Acoustic emission and ultrasonic transmission monitoring of hydraulic fracture propagation in heterogeneous rock samples. In: 46th U.S. rock mechanics/geomechanics symposium, American Rock Mechanics Association

Stanchits S, Burghardt J, Surdi A (2015) Hydraulic fracturing of heterogeneous rock monitored by acoustic emission. Rock Mech Rock Eng 48(6):2513–2527

Thiercelin M, Roegiers JC, Boone TJ, Ingraffea AR (1987) An investigation of the material parameters that govern the behavior of fractures approaching rock interfaces. In: 6th ISRM congress, International Society for Rock Mechanics

Wang DB, Zhou FJ, Ge HK, Shi Y, Yi XY, Xiong CM, Liu XF, Wu YQ, Li Y (2015) An experimental study on the mechanism of

degradable fiber-assisted diverting fracturing and its influencing factors. J Nat Gas Sci Eng 27(1):260–273

Warpinski NR, Branagan PT (1989) Altered-stress fracturing. J Pet Technol 41(9):990–997

Warpinski NR, Teufel LW (1984) Influence of geologic discontinuities on hydraulic fracture propagation. J Pet Technol 39(2):209–220

Warpinski NR, Mayerhofer M, Agarwal K, Du J (2013) Hydraulic-fracture geomechanics and microseismic-source mechanisms. SPE J 18(4):766–780

Weng X, Kresse O, Cohen CE, Wu R, Gu H (2011) Modeling of hydraulic fracture network propagation in a naturally fractured formation. SPE Prod Oper 26(4):368–380

Zang A, Wagner FC, Stanchits S, Dresen G, Andresen R, Haidekker MA (1998) Source analysis of acoustic emissions in aue granite cores under symmetric and asymmetric compressive loads. Geophys J Int 135(3):1113–1130

Zhang X, Jeffrey RG (2007) Hydraulic fracture propagation across frictional interfaces. In: 1st Canada-U.S. rock mechanics symposium, American Rock Mechanics Association

Zhou J, Chen M, Jin Y, Zhang GQ (2008) Analysis of fracture propagation behavior and fracture geometry using a tri-axial fracturing system in naturally fractured reservoirs. Int J Rock Mech Min Sci 45(7):1143–1152

Zhou FJ, Liu YZ, Yang XY, Zhang FX, Xiong CM, Liu XF (2009) Case study: YM204 obtained high petroleum production by acid fracture treatment combining fluid diversion and fracture reorientation. In: 8th European formation damage conference, Society of Petroleum Engineers

Zhu QZ (2017) A new rock strength criterion from microcracking mechanisms which provides theoretical evidence of hybrid failure. Rock Mech Rock Eng 50(2):341–352

Zou YS, Zhang SC, Zhou T, Zhou X, Guo TK (2016a) Experimental investigation into hydraulic fracture network propagation in gas shales using CT scanning technology. Rock Mech Rock Eng 49(1):33–45

Zou YS, Ma XF, Zhang SC, Zhou T, Li H (2016b) Numerical investigation into the Influence of bedding plane on hydraulic fracture network propagation in shale formations. Rock Mech Rock Eng 49(9):3597–3614

Zou YS, Ma XF, Zhou T, Li N, Chen M, Li SH, Zhang YN, Li H (2017) Hydraulic fracture growth in a layered formation based on fracturing experiments and discrete element modeling. Rock Mech Rock Eng 50(9):2381–2395